Fusion of Multiple Images by Higher-Order SVD of Third-Order Image Tensors

Michael Thomason and Jens Gregor
{*thomason,jgregor*}*@cs.utk.edu*
Department of EECS
203 Claxton Complex
University of Tennessee
Knoxville, TN 37996

Technical Report ut-cs-07-607

November 28, 2007

Abstract

An important topic in image fusion is methodology to combine multiple digital images for visual display or for processing such as traditional edge detection or data mining to find image-related structure. This paper describes a method of fusion for applications in which (1) input images have been registered, sized, and scaled in pixel intensities suitably for mutual comparison (for example, inputs from a multi-lens array), and (2) information about edges and lines is desired. The fusion is a sequence of computations. The first step organizes the input images as a third-order tensor $\mathcal{A}$ and computes a higher-order generalization of singular value decomposition (abbreviated HOSVD) for $\mathcal{A}$. HOSVD creates a subtensor $\mathcal{B}$ containing a set of images that are linear fusions of the inputs, orthogonal, and ordered by decreasing norm. The second step is phase analysis of the basis images in $\mathcal{B}$ which extracts edge-line information by computing image phase maps. The third step fuses the raw phase maps themselves by local energy criteria, i.e., by pixel-wise square root of the sum of the squares. Finally, the fused maps are combined with input images for visualization and can be used in other processing, for instance, to delineate regions by connected line segments. In some applications additional input images are acquired after the initial HOSVD, in which case incremental HOSVD is an effective way to update an existing decomposition without recomputing the entire HOSVD from scratch. Reduced dimension HOSVD is an option for reducing the storage requirements but introduces an error that must be acceptable in an application. Examples of fusion are given using multimodal images and multiresolution images.

Keywords: basis images, HOSVD, image fusion, incremental HOSVD, phase analysis, reduced dimension HOSVD, tensor

1 Introduction

Image fusion develops methods to combine multiple digitized inputs for visualization (often as single images) or for processing such as traditional edge detection or data mining to find image-related structure. Recent work in image fusion includes imaging from multiple exposures [12] or multiple depths of focus [20], suppression of cloud covering [9], pre-fusion registration based on line and point features [24], visible and thermal images for face recognition [2, 16], multimodal images in non-destructive testing [23], multispectral and multiresolution data in remote sensing [11, 21, 29],

and multimodal medical images in rare but important neurological cases [28]. Methods based on wavelets [21, 22, 25] and mathematical statistics [3, 4] are popular.

This paper describes a method of digital image fusion for applications in which (1) 2-D inputs have been registered, sized, and scaled in pixel intensities appropriately for mutual comparison, and (2) ensemble information in the form of edges and lines is desired. An example of this kind of application is a system with inputs from a multi-lens array (cf. [26, 30]) that acquires multiple images of the same object or scene through different spectral filters.

The method is a sequence of computations. It decomposes the input images into a common basis set, analyzes the basis images to extract ensemble edge-line details, and then fuses the results of the analysis. The output of this pipeline is a set of fused phase maps, in the form of 2-D images, that are the explicit edge-line information.

At the start of this pipeline, the first task is to organize the input images into a multilinear array which is a *third-order tensor* $\mathcal{A}$ and compute a higher-order generalization of singular value decomposition (SVD) for $\mathcal{A}$. This *higher-order decomposition*, abbreviated HOSVD, creates a subtensor $\mathcal{B}$ containing a set of images that are orthogonal, are ordered by decreasing norm, and constitute a basis for the inputs. Each basis image is a linear fusion of the input images. The second task is phase analysis of each basis image to extract information about edges and lines. The third task fuses the raw phase maps by pixel-wise square root of the sum of the squares—a computation consistent with the role of local energy in image phase analysis. Finally, the fused maps are added to input images for purposes of visualization. They can also be used in other processing in which edge-line information is relevant.

The paper is organized as follows. Section 2.1 defines the subtensor $\mathcal{B}$ of basis images computed from tensor $\mathcal{A}$ by HOSVD. Post-HOSVD *image phase analysis* to find edges and lines in the images in $\mathcal{B}$ is described in section 2.2 and illustrated in the examples in section 3. In some applications, additional input images are acquired after HOSVD has been computed for an initial set of images, in which case the decomposition must be updated to include the new data. *Incremental* HOSVD for this task is described in section 2.3 and computed in sections 3.1 and 3.2. *Reduced dimension* HOSVD is a well known method for reducing storage requirements at the cost of introducing error in the decomposition. For completeness, it is discussed in section 2.4 and illustrated in section 3.1.3.

2 Third-Order Image Tensors and HOSVD

2.1 Tensor $\mathcal{A}$, HOSVD, and Subtensor $\mathcal{B}$

Tensor-based image processing is an active area of research (cf. [31, 32, 33]). Mathematically speaking, *tensors* are higher-order equivalents of scalars (zeroth order), one-index vectors (first order), and two-index matrices (second order). Notation and several important properties of tensor computations [1, 7, 8] are summarized in the appendix.

When a set of 2-D, grayscale images of the same size is organized as a third-order tensor $\mathcal{A}$, HOSVD [8] is a powerful decomposition tool. Let $\Theta_1, \Theta_2, \ldots, \Theta_{I_1}$ denote a set of I_1 images, each one a $I_2 \times I_3$ matrix of pixels, registered and scaled in intensity suitable for the application. To organize these input images as a single tensor, they are stacked along dimension 1 to create $(I_1 \times I_2 \times I_3)$-tensor $\mathcal{A}$. The $(1 \times I_2 \times I_3)$-subtensor $\mathcal{A}_{i_1=i}$ obtained from $\mathcal{A}$ by fixing the first index i_1 to i is the tensor version of $(I_2 \times I_3)$-image Θ_i.

The decomposition of tensor $\mathcal{A}$ by HOSVD is represented in figure 1. $\mathcal{A}$ equals the core tensor $\mathcal{S}$ times the three n-mode matrices of left singular vectors:

$$\begin{aligned} \mathcal{A} &= \mathcal{S} \times_1 \mathbf{U}^{(1)} \times_2 \mathbf{U}^{(2)} \times_3 \mathbf{U}^{(3)} \\ &= \left(\mathcal{S} \times_2 \mathbf{U}^{(2)} \times_3 \mathbf{U}^{(3)}\right) \times_1 \mathbf{U}^{(1)} \\ &= \mathcal{B} \times_1 \mathbf{U}^{(1)} \end{aligned}$$

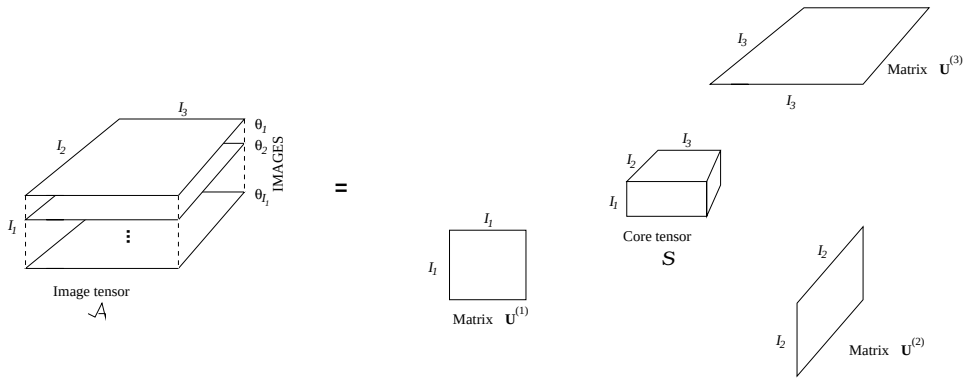

Figure 1: HOSVD: $(I_1 \times I_2 \times I_3)$-tensor $\mathcal{A}$ equals $\mathcal{S} \times_1 \mathbf{U}^{(1)} \times_2 \mathbf{U}^{(2)} \times_3 \mathbf{U}^{(3)}$.

where $\times_n$ denotes a tensor-times-matrix product and the subtensor $\mathcal{B} = \mathcal{S} \times_2 \mathbf{U}^{(2)} \times_3 \mathbf{U}^{(3)}$ defines a 2-D basis set for the original images. Both $\mathcal{B}$ and the core tensor $\mathcal{S}$ are size $I_1 \times I_2 \times I_3$, the 1-mode matrix $\mathbf{U}^{(1)}$ is $I_1 \times I_1$, the 2-mode matrix $\mathbf{U}^{(2)}$ is $I_2 \times I_2$, and the 3-mode matrix $\mathbf{U}^{(3)}$ is $I_3 \times I_3$. The original image subtensors are thereby decomposed in the linear form

$$\mathcal{A}_{i_1=i} = \mathcal{B} \times_1 \mathbf{U}^{(1)}(i,:)$$

where $\mathbf{U}^{(1)}(i,:)$ is row i in matrix $\mathbf{U}^{(1)}$. The tensor-times-matrix product $\mathcal{B} \times_1 \mathbf{U}^{(1)}(i,:)$ has the correct size $1 \times I_2 \times I_3$ because it is an $(I_1 \times I_2 \times I_3)$-tensor times a $(1 \times I_1)$-matrix. For simpler notation, we write

u_{ij} for the scalar $\mathbf{U}^{(1)}(i,j)$ and $[u_{i1}\ u_{i2} \dots\ u_{iI_1}]$ for row i in $\mathbf{U}^{(1)}$,

β_j for the $(1 \times I_2 \times I_3)$-subtensor $\mathcal{B}_{i_1=j}$, and

$\mathbf{b}_j$ for the $(I_2 \times I_3)$-matrix version of β_j.

Conversion between $(1 \times I_2 \times I_3)$-subtensors and ordinary $(I_2 \times I_3)$-matrices is straightforward (essentially by deleting or adding array dimension I_1). In matrix form, the decomposition of the original image Θ_i is

$$\begin{aligned} \Theta_i &= u_{i1}\mathbf{b}_1 + u_{i2}\mathbf{b}_2 + \cdots + u_{iI_1}\mathbf{b}_{I_1} \\ &= \sum_{j=1}^{I_1} u_{ij}\mathbf{b}_j. \end{aligned}$$

Due to the properties of HOSVD, both the rows of matrix $\mathbf{U}^{(1)}$ and its columns are orthonormal. The subtensors β_j are orthogonal,

$$\langle \beta_j, \beta_k \rangle = 0 \text{ if } j \neq k$$

where $\langle$-,-$\rangle$ denotes the scalar product of two tensors of the same size, and are ordered by decreasing norm,

$$||\beta_1|| \geq ||\beta_2|| \geq \cdots \geq ||\beta_{I_1}||.$$

Numerically, the coefficient u_{ij} is

$$u_{ij} = \frac{\langle \mathcal{A}_{i_1=i}, \beta_j \rangle}{||\beta_j||^2},$$

an equation familar in linear analysis for projection of a vector to a subspace [17]. In fact, given any $(1 \times I_2 \times I_3)$-tensor $\mathcal{Z}$, the linear combination of the subtensors β_j closest to $\mathcal{Z}$ in the least squares sense has coefficients

$$c_j = \frac{\langle \mathcal{Z}, \beta_j \rangle}{||\beta_j||^2} \quad \text{for} \quad 1 \leq j \leq I_1.$$

Since the inverse of orthogonal matrix $\mathbf{U}^{(1)}$ is its transpose $\mathbf{U}^{(1)^T}$, the basis images β_j themselves are unique linear combinations of the original images, expressed by the tensor equation

$$\mathcal{B} = \mathcal{A} \times_1 \mathbf{U}^{(1)^T}$$

or in matrix form for individual image $\mathbf{b}_j$ as

$$\mathbf{b}_j = \sum_{i=1}^{I_1} u_{ij} \Theta_i.$$

2.2 Image Phase Analysis for Edge and Line Detection

After HOSVD of tensor $\mathcal{A}$ has been computed, the basis images in subtensor $\mathcal{B}$ are available for analysis. We use frequency phase analysis of images [18, 19] to extract information about edges and lines. The phase analysis map of an $(I_2 \times I_3)$-image is an $(I_2 \times I_3)$-image of scaled real numbers, not hard-thresholded binary, and tends to be robust with respect to variations in contrast and luminance.

Phase congruency and *phase symmetry analysis* compute the frequency components via a transform such as 2-D Gabor wavelets of pixel intensities, then analyze the relative phases of the frequency components locally [18, 19]. Phase congruency assigns numbers that are proportional to the amount of local in-phase agreement in the frequency components [18]. Phase symmetry assigns higher numbers (more symmetry) where frequency components are nearer to their maximum or minimum cycle points and lower numbers (less symmetry) where frequency components are nearer to the inflection points in their cycles [19]. Phase symmetry is a specialized search for symmetries and partial symmetries in structure, whereas phase congruency is less specific. In practice, our choice between them is empirical: we compute both and opt for the one delivering more visual detail about edges and lines in a given application.

The phase maps themselves are $(I_2 \times I_3)$-images amenable to fusion. An approach well adapted to many applications is to fuse the raw phase maps of images in $\mathcal{B}$ by pixel-wise square root of the sum of the squares. This is consistent with the role of local energy in phase analysis. In the examples in section 3, the phase maps are computed with default values of control parameters [18, 19] and are fused in this way. Subsequently, the fused phase maps can be combined with other images by image addition, with the fused maps being rescaled if desired for visualization.

A particular application might also mandate further processing to satisfy various requirements. For example, processing might be required to suppress non-maximal values in raw phase maps, find connected line segments and convert them into binary maps by hard thresholding, and finally combine the binary maps with input images to delineate distinct regions. Application-orientated processing of this kind is not covered in this paper.

2.3 HOSVD Updating with Additional Data

In some applications, additional input images are acquired after HOSVD has been computed. If the HOSVD of $(I_1 \times I_2 \times I_3)$-tensor $\mathcal{A}$ has already been computed and another input image Θ_{I_1+1} is obtained, then the existing decomposition must be updated by incorporating the new $(I_2 \times I_3)$-image Θ_{I_1+1} and incrementing dimension I_1. Two options are (1) recompute the entire HOSVD on an upsized $([I_1 + 1] \times I_2 \times I_3)$-tensor or (2) incrementally update the existing decomposition.

The second option is motivated by *incremental SVD or SVD updating* in conventional SVD [5]. The updating algorithm in SVD takes an existing decomposition $\mathbf{USV}^T$, projects the new 2-D matrix $\mathbf{Z}$ onto the subspace spanned by $\mathbf{U}$ and onto the orthogonal subspace $\mathbf{H}$ in which the component of $\mathbf{Z}$ perpendicular to $\mathbf{U}$ lies, finds an orthogonal basis for $\mathbf{H}$, and updates the SVD to account for the components in subspace $\mathbf{H}$ as well as the changes in $\mathbf{U}$. If the projection onto $\mathbf{H}$ is less than some small threshold, truncation to 0 is suggested for noise supression [5].

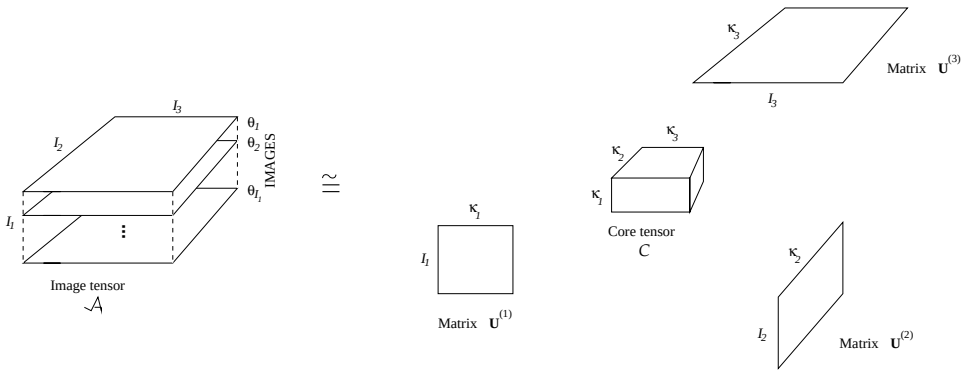

Figure 2: Reduced Dimension HOSVD: Tensor $\mathcal{A}$ approximated by $\hat{\mathcal{A}} = \mathcal{C} \times_1 \mathbf{U}^{(1)} \times_2 \mathbf{U}^{(2)} \times_3 \mathbf{U}^{(3)}$.

Incremental SVD can be significantly faster than recomputing the entire SVD. (In big O notation, if $\mathbf{M}$ is a $(d \times N)$-matrix of N samples of $d \times 1$ data vectors, then standard SVD of $\mathbf{M}$ has time complexity $O(d^2N + dN^2 + N^3)$ whereas incremental updating to incorporate a $(d \times c)$-matrix of c new data vectors has time complexity $O(d^3 + dc^2)$ [5].) Our method for incremental HOSVD has two parts: first update the three matrices $\mathbf{U}^{(1)}$, $\mathbf{U}^{(2)}$, $\mathbf{U}^{(3)}$ by computing incremental SVD separately on the unfolded matrices $\mathbf{A}_{(1)}$, $\mathbf{A}_{(2)}$, $\mathbf{A}_{(3)}$, then compute the new core tensor

$$\bar{\mathcal{S}} = \bar{\mathcal{A}} \times_1 \bar{\mathbf{U}}^{(1)^T} \times_2 \bar{\mathbf{U}}^{(2)^T} \times_3 \bar{\mathbf{U}}^{(3)^T}$$

where the bar denotes updated values. This simultaneously updates the basis images by creating a new subtensor $\bar{\mathcal{B}} = \bar{\mathcal{S}} \times_2 \bar{\mathbf{U}}^{(2)} \times_3 \bar{\mathbf{U}}^{(3)}$.

2.4 Reduced Dimension HOSVD

Reduced dimension HOSVD is concerned with finding the best rank-$(\kappa_1 \times \kappa_2 \times \cdots \times \kappa_N)$ approximation of a given $(I_1 \times I_2 \times \cdots \times I_N)$-tensor $\mathcal{A}$. A reduced dimension decomposition has a smaller core tensor and at least one smaller n-mode matrix as shown in figure 2, but still defines an approximation $\hat{\mathcal{A}}$ identical in size to $\mathcal{A}$. The *best approximation* in the least squares sense minimizes the mean squared error (MSE) $||\mathcal{A} - \hat{\mathcal{A}}||^2$ [8].

A well known method for finding an optimal approximation is *higher-order orthogonal iteration* (HOOI) [8]. HOOI is an alternating least squares method that makes repeated passes through the reduced-size n-mode matrices $\mathbf{U}^{(1)}$, $\mathbf{U}^{(2)}$, ..., $\mathbf{U}^{(N)}$. Each pass steps through all N-modes, optimizing one n-mode matrix at a time while the others are held constant. In practice, iteration continues until a relevant measure of error in the approximation falls below a threshold value or stabilizes with no sign of decreasing further. The example in section 3.1 lists the relative norm $||\mathcal{A} - \hat{\mathcal{A}}||/||\mathcal{A}||$ and also a structural similarity index [34] designed to take visual characteristics of images into account. Reduced dimension HOSVD is a trade-off between smaller storage and the amount of error acceptable in an application.

3 Examples

Two examples using third-order tensors and HOSVD are given here. The first illustrates multimodal images in non-destructive testing. The second illustrates lower resolution satellite data fused with aerial photography at a higher resolution.

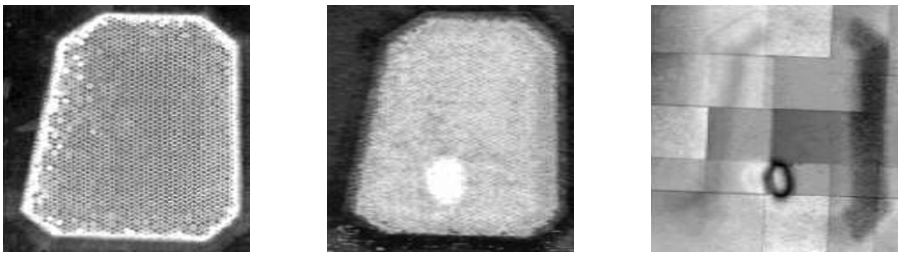

(a) (b) (c)

Figure 3: Multimodal images [23]: (a) Θ_1 X-ray, (b) Θ_2 ultrasound, (c) Θ_3 shearography. Courtesy AIPnD (The Italian Society for Non-Destructive Testing Monitoring Diagnostics).

3.1 Multiple Image Modalities

Multimodal images are used in non-destructive testing. The three images in figure 3 are (a) Θ_1 *X-ray*, (b) Θ_2 *ultrasound*, and (c) Θ_3 *shearography* for part of an aircraft component [23]. Shearography is a laser-based method for visual detection of surface deformations without the use of contact devices such as strain gauges. The images in figure 3 are 256×256, 8-bit (0:255) grayscale pixels, already registered by a preprocessing step [23]. Visible in the X-ray image is a carbon-fiber honeycomb pattern. The ultrasound and shearography images reveal a defect near the bottom of the structure. Although a three-image tensor incorporating Θ_1, Θ_2 and Θ_3 could be formed at once, this example begins with a two-image tensor and illustrates incremental HOSVD to incorporate the third image.

3.1.1 X-Ray and Ultrasound Data

As described in section 2.1, the $(2 \times 256 \times 256)$-tensor $\mathcal{A}$ is created such that the subtensor $\mathcal{A}_{i_1=1}$ is the X-ray image Θ_1 and the subtensor $\mathcal{A}_{i_1=2}$ is the ultrasound image Θ_2. The HOSVD of $\mathcal{A}$ is

$$\begin{aligned} \mathcal{A} &= \mathcal{S} \times_1 \mathbf{U}^{(1)} \times_2 \mathbf{U}^{(2)} \times_3 \mathbf{U}^{(3)} \\ &= \mathcal{B} \times_1 \mathbf{U}^{(1)} \end{aligned}$$

where tensors $\mathcal{A}$, $\mathcal{S}$, and $\mathcal{B}$ all have size $2 \times 256 \times 256$, matrices $\mathbf{U}^{(2)}$ and $\mathbf{U}^{(3)}$ are 256×256, and the 2×2 matrix of 1-mode coefficients is

$$\mathbf{U}^{(1)} = \begin{bmatrix} 0.6988 & 0.7154 \\ 0.7154 & -0.6988 \end{bmatrix}.$$

Figures 4(a) and 4(b) are the basis images $\mathbf{b}_1$ and $\mathbf{b}_2$, the matrix versions of the subtensors $\beta_1 = \mathcal{B}_{i_1=1}$ and $\beta_2 = \mathcal{B}_{i_1=2}$. The norms are decreasing:

$$||\beta_1|| = 5.97\text{e+}04 > ||\beta_2|| = 9.81\text{e+}03.$$

Figures 4(c) and 4(d) are the raw phase symmetry maps denoted by $\mathbf{p}_1$ for $\mathbf{b}_1$ and $\mathbf{p}_2$ for $\mathbf{b}_2$. Figure 4(e) is the fusion of $\mathbf{p}_1$ and $\mathbf{p}_2$ by pixel-wise square root of the sum of the squares, denoted by $f(\mathbf{p}_1, \mathbf{p}_2)$.

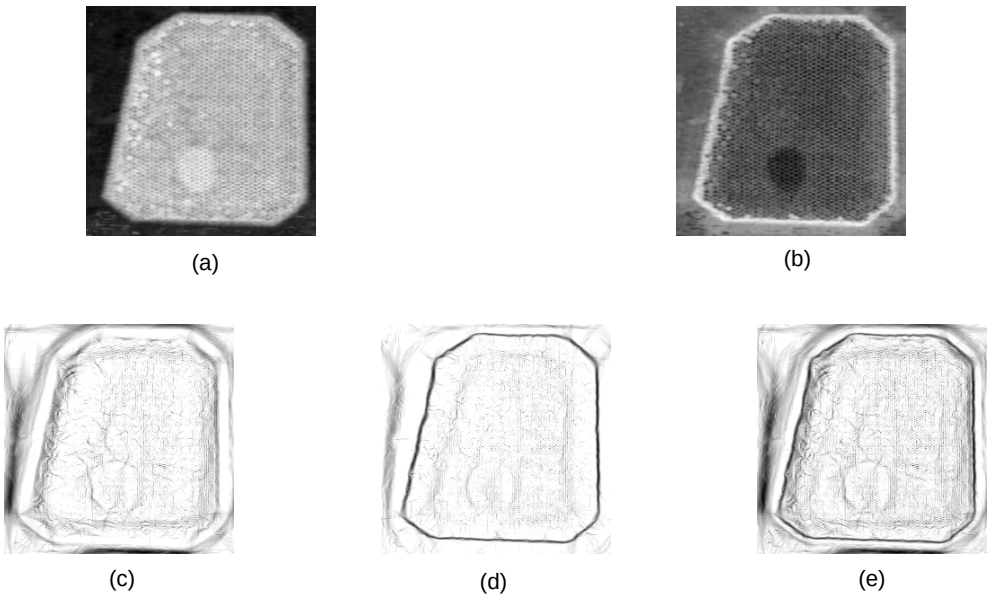

Figure 4: Matrices in two-image $\mathcal{B}$: (a) $\mathbf{b}_1$, (b) $\mathbf{b}_2$. Phase symmetry maps: (c) $\mathbf{p}_1$, (d) $\mathbf{p}_2$, (e) fusion $f(\mathbf{p}_1, \mathbf{p}_2)$.

The reconstructions of the X-ray and ultrasound images are the respective linear forms

$$\Theta_1 \approx 0.6988\mathbf{b}_1 + 0.7154\mathbf{b}_2 \quad \text{and} \quad \Theta_2 \approx 0.7154\mathbf{b}_1 - 0.6988\mathbf{b}_2.$$

Since the four coefficients u_{ij} for these particular images are about the same magnitude, namely $|u_{ij}| \approx 0.7$, the image $\mathbf{b}_2$ is essentially an adjustment added to $\mathbf{b}_1$ to reproduce Θ_1 and subtracted to reproduce Θ_2. The linear forms are visually indistinguishable from Θ_1 and Θ_2 when printed as images. In quantitative terms, the MSE between each of Θ_1 and Θ_2 and its linear form respectively is 2.42e-08 and 2.80e-08. MSE is not always a good measure of visual differences [10], so we also compute a structural similarity index [34] designed to account for illumination, contrast, and local pixel intensities. This index, which is normalized from 0 (worst comparatively) to 1 (best), has performed well in empirical testing with subjective assessment of visual differences [34]. Using the default settings of its control parameters [34], the index value is 1 between each of Θ_1 and Θ_2 and its linear form. For reference, the index is 0.1512 between Θ_1 and Θ_2 themselves.

3.1.2 Updating with Shearography Data

The shearography image Θ_3 is incorporated by incremental HOSVD described in section 2.3, i.e., the existing HOSVD for Θ_1 and Θ_2 is updated to incorporate Θ_3. The updated 3×3 matrix of coefficients is

$$\bar{\mathbf{U}}^{(1)} = \begin{bmatrix} 0.5850 & 0.2423 & -0.7740 \\ 0.5940 & 0.5218 & 0.6123 \\ 0.5523 & -0.8179 & 0.1613 \end{bmatrix}$$

and the norms of the new subtensors in the updated $\bar{\mathcal{B}}$ are

$$||\bar{\beta}_1|| = 7.10\text{e}{+04}, \quad ||\bar{\beta}_2|| = 1.51\text{e}{+04}, \quad ||\bar{\beta}_3|| = 9.55\text{e}{+03}.$$

Figures 5(a)-(b)-(c) are the new matrices $\bar{\mathbf{b}}_1$, $\bar{\mathbf{b}}_2$, and $\bar{\mathbf{b}}_3$. Figure 5(d) is the raw phase map $\bar{\mathbf{p}}_1$ for image $\bar{\mathbf{b}}_1$ alone; 5(e) is $f(\bar{\mathbf{p}}_1, \bar{\mathbf{p}}_2)$, the fusion of the maps $\bar{\mathbf{p}}_1$ and $\bar{\mathbf{p}}_2$; and 5(f) is $f(\bar{\mathbf{p}}_1, \bar{\mathbf{p}}_2, \bar{\mathbf{p}}_3)$, the fusion of all three phase maps.

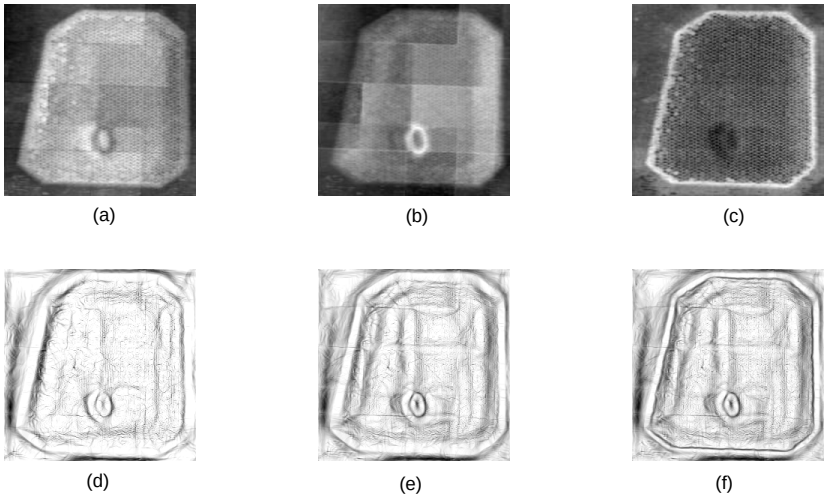

Figure 5: Matrices in three-image $\bar{\mathcal{B}}$: (a) $\bar{\mathbf{b}}_1$, (b) $\bar{\mathbf{b}}_2$, (c) $\bar{\mathbf{b}}_3$. Phase symmetry maps: (d) $\bar{\mathbf{p}}_1$, (e) fusion $f(\bar{\mathbf{p}}_1, \bar{\mathbf{p}}_2)$, (f) fusion $f(\bar{\mathbf{p}}_1, \bar{\mathbf{p}}_2, \bar{\mathbf{p}}_3)$.

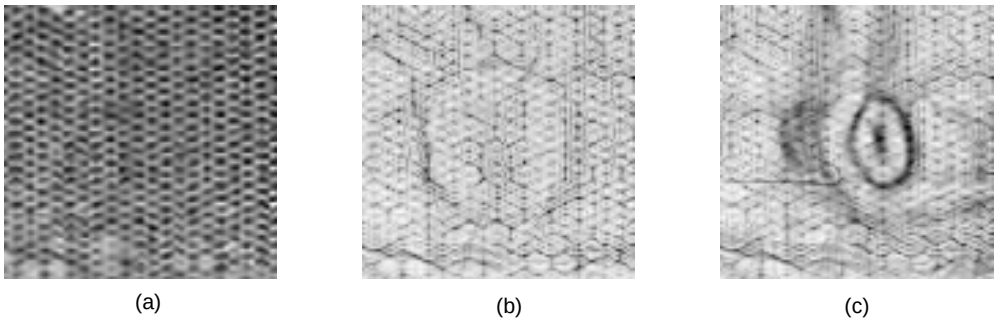

Figure 6: ROI containing the defect: (a) Θ_1 X-ray, (b) X-ray plus $f(\mathbf{p}_1, \mathbf{p}_2)$, (c) X-ray plus $f(\bar{\mathbf{p}}_1, \bar{\mathbf{p}}_2, \bar{\mathbf{p}}_3)$.

Figure 6(a) shows a (100×100)-pixel region of interest (ROI) containing the defect in the X-ray image Θ_1. There is little or no visible hint of the defect. Figure 6(b) adds the fused phase map $f(\mathbf{p}_1, \mathbf{p}_2)$ to the X-ray ROI. This is a fusion of X-ray and ultrasound data only. As described above, the existing two-image HOSVD is updated by incremental HOSVD to incorporate the shearography image. Figure 6(c) adds the fused map $f(\bar{\mathbf{p}}_1, \bar{\mathbf{p}}_2, \bar{\mathbf{p}}_3)$ to the X-ray ROI. This is the fusion to which all three image modalities contribute.

3.1.3 Reduced Dimension HOSVD

There is an opportunity to reduce the storage needed for the core tensor $\mathcal{S}$ and the n-mode matrices $\mathbf{U}^{(1)}$, $\mathbf{U}^{(2)}$, $\mathbf{U}^{(3)}$ by reduced dimension HOSVD described in section 2.4. Reducing the dimension of HOSVD is a trade-off between smaller storage and the error introduced by the approximation; however, substantially reduced dimensions may cause relatively small visual differences as measured by the structural similarity index. HOOI is computed here to approximate the $(3 \times 256 \times 256)$-tensor $\mathcal{A}$ by three reduced sizes: $3 \times 100 \times 100$, $3 \times 100 \times 50$, and $3 \times 50 \times 100$. The iteration was terminated when the norm of the difference in updating each n-mode matrix $\mathbf{U}^{(n)}$ became less than 1e-10.

The norm of tensor $\mathcal{A}$ is $||\mathcal{A}|| = 7.32\text{e+}04$ and its energy is $||\mathcal{A}||^2 = 5.36\text{e+}09$. The following lists the relative norms and the storage for the approximations $\hat{\mathcal{A}}$. Storage is bytes as a percentage of the full HOSVD (2,621,964 bytes).

Size	$3 \times 100 \times 100$	$3 \times 100 \times 50$	$3 \times 50 \times 100$
$\|\|\mathcal{A} - \hat{\mathcal{A}}\|\|/\|\|\mathcal{A}\|\|$	0.0127	0.0233	0.0282
Storage	24.8%	16.3%	16.3%

The structural similarity index [34] computed in section 3.1.1 is one measure of visible error introduced by the reduction. The following tabulates the index between each image Θ_1, Θ_2, Θ_3 and its linear form from the approximation $\hat{\mathcal{A}}$.

Size	$3 \times 100 \times 100$	$3 \times 100 \times 50$	$3 \times 50 \times 100$
Θ_1 X-ray	0.9877	0.9579	0.8805
Θ_2 ultrasound	0.9742	0.9290	0.9476
Θ_3 shearography	0.9772	0.9537	0.9319

For reference, the index between Θ_1 and Θ_2 is 0.1512, between Θ_1 and Θ_3 is 0.1514, and between Θ_2 and Θ_3 is 0.3151. This index computed between the images in $\mathcal{B}$ and in the approximations $\hat{\mathcal{B}}$ measures the visual deterioration in the basis images due to reduced dimensions:

Size	$3 \times 100 \times 100$	$3 \times 100 \times 50$	$3 \times 50 \times 100$
Between $\mathbf{b}_1$ and $\widehat{\mathbf{b}}_1$	0.9844	0.9530	0.9331
Between $\mathbf{b}_2$ and $\widehat{\mathbf{b}}_2$	0.9801	0.9469	0.9159
Between $\mathbf{b}_3$ and $\widehat{\mathbf{b}}_3$	0.9848	0.9456	0.9243

3.2 Multiresolution Images

The use of higher resolution panchromatic image data to "pan-sharpen" lower resolution multispectral data is well established in remote sensing [27]. A complementary way of fusing and displaying

(a) (b) (c)

Figure 7: D.C. images: (a) Θ_1 ASTER (15 meter), (b) Θ_2 Landsat (15 meter), (c) Θ_3 aerial photography (1 meter). Credits: (a) is a rotated subimage of a larger image at NASA/GSFC/METI/ERSDAC/JAROS; (b) and (c) are subimages of larger images at NASA/Goddard Space Fight Center.

edge-line information is to use HOSVD to create optimal subtensor $\mathcal{B}$, fuse the raw phase maps of images in $\mathcal{B}$, and add the fused maps to low resolution images for visualization.

Figure 7 shows three images of Washington, D.C., USA, with the Washington Monument roughly at the center. These are manually registered subimages of larger images, converted to 8-bit grayscale and resized to 256×256 pixels for this example. Figure 7(a) Θ_1 is a combination of visible and near infrared bands from ASTER, a US/Japan Advanced Spaceborne Thermal Emission and Reflection Radiometer, at 15 meter resolution. Figure 7(b) Θ_2 is a Landsat image pan-sharpended to 15 meter resolution, i.e, panchromatic data has already been used to sharpen the edges in multispectral bands to produce the image at that resolution. Figure 7(c) Θ_3 is aerial photography at 1 meter resolution. For reference as a measure of visual differences, the structural similarity index [34] is 0.3591 between Θ_1 and Θ_2, 0.1730 between Θ_1 and Θ_3, and 0.2423 between Θ_2 and Θ_3.

The $(2 \times 256 \times 256)$-tensor $\mathcal{A}$ is created with subtensor $\mathcal{A}_{i_1=1} = \Theta_1$, the ASTER image, and subtensor $\mathcal{A}_{i_1=2} = \Theta_2$, the Landsat image. The HOSVD of $\mathcal{A}$ is

$$\begin{aligned} \mathcal{A} &= \mathcal{S} \times_1 \mathbf{U}^{(1)} \times_2 \mathbf{U}^{(2)} \times_3 \mathbf{U}^{(3)} \\ &= \mathcal{B} \times_1 \mathbf{U}^{(1)} \end{aligned}$$

where the 2×2 matrix of 1-mode coefficients is

$$\mathbf{U}^{(1)} = \begin{bmatrix} 0.6926 & -0.7213 \\ 0.7213 & 0.6926 \end{bmatrix}$$

and the subtensor norms are

$$||\beta_1|| = 4.91\text{e+}04 > ||\beta_2|| = 8.41\text{e+}03.$$

The two-image HOSVD is updated with image Θ_3 by incremental HOSVD described in section 2.3.

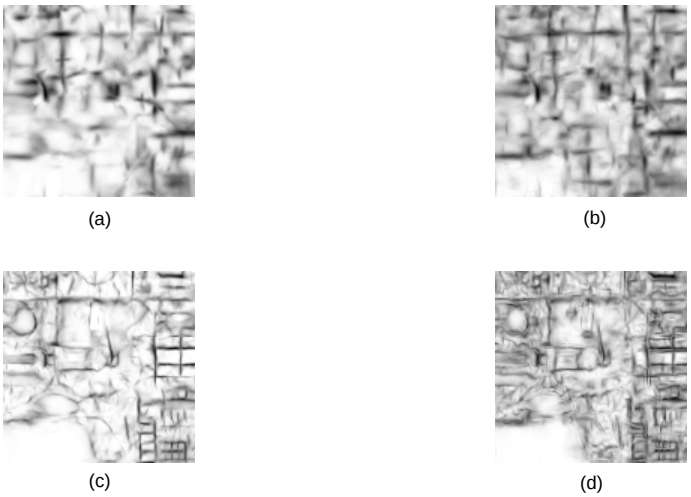

Figure 8: Phase congruency maps in ROI: (a) $\mathbf{p}_1$, (b) fusion $f(\mathbf{p}_1, \mathbf{p}_2)$, (c) $\bar{\mathbf{p}}_1$, (d) fusion $f(\bar{\mathbf{p}}_1, \bar{\mathbf{p}}_2, \bar{\mathbf{p}}_3)$.

The updated 3×3 matrix of coefficients is

$$\bar{\mathbf{U}}^{(1)} = \begin{bmatrix} 0.6061 & 0.5708 & 0.5539 \\ 0.6359 & 0.0706 & -0.7686 \\ -0.4778 & 0.8180 & -0.3202 \end{bmatrix}$$

and the updated subtensor norms are

$$||\bar{\beta}_1|| = 5.56\text{e+}04, \;\; ||\bar{\beta}_2|| = 1.08\text{e+}04, \;\; ||\bar{\beta}_3|| = 7.98\text{e+}03.$$

The phase congruency maps in figure 8 give an overall visual impression of the edge and line details in subtensors $\mathcal{B}$ and $\bar{\mathcal{B}}$ within a (128×128)-pixel ROI in which the Washington Monument is approximately centered. Figure 8(a) is the raw phase map for $\mathbf{b}_1$, the image with the larger norm in the two-image subtensor $\mathcal{B}$, and figure 8(b) is $f(\mathbf{p}_1, \mathbf{p}_2)$, the fusion of the phase maps $\mathbf{p}_1$ and $\mathbf{p}_2$ by pixel-wise square root of the sum of the squares. This is a fusion of information from ASTER and Landsat images. Figure 8(c) is the phase map for $\bar{\mathbf{b}}_1$, the image with largest norm in the three-image subtensor $\bar{\mathcal{B}}$. Figure 8(d) is $f(\bar{\mathbf{p}}_1, \bar{\mathbf{p}}_2, \bar{\mathbf{p}}_3)$, the fusion of all three phase maps incorporating high resolution information from aerial photography with the other two.

Figure 9(a) is the ROI in Θ_1, the ASTER image. Figures 9(b) and 9(c) are the ASTER ROI with the addition of the fused phase maps $f(\mathbf{p}_1, \mathbf{p}_2)$ and $f(\bar{\mathbf{p}}_1, \bar{\mathbf{p}}_2, \bar{\mathbf{p}}_3)$ respectively. Figure 9(d) is the ROI in Θ_2, the Landsat image. Figures 9(e) and 9(f) are the Landsat ROI to which are added the fused maps $f(\mathbf{p}_1, \mathbf{p}_2)$ and $f(\bar{\mathbf{p}}_1, \bar{\mathbf{p}}_2, \bar{\mathbf{p}}_3)$ respectively. Figures 9(b) and 9(e) are fusions of ASTER and Landsat data only. Figures 9(c) and 9(f) are fusions of the high resolution image with the other two.

The examples in this paper use the fused phase maps without attempting, for instance, to suppress noise artifacts or to define binary edge-line maps by thresholding. The four images of the ROI in figure 10 give a brief example only of further image processing of a traditional nature, specifically, gradients in Canny edge detection [6] computed for fused phase maps. The gradient maps are computed using a Gaussian smoothing filter with standard deviation 1 but without subsequent hysteresis thresholding [6] to derive binary images, and are added to the ASTER and Landsat input images. Figures 10(a) and 10(b) respectively are the edge gradient maps of $f(\mathbf{p}_1, \mathbf{p}_2)$ and $f(\bar{\mathbf{p}}_1, \bar{\mathbf{p}}_2, \bar{\mathbf{p}}_3)$ added to the ASTER ROI. Figures 10(c) and 10(d) are the same edge gradient maps respectively added to the Landsat ROI.

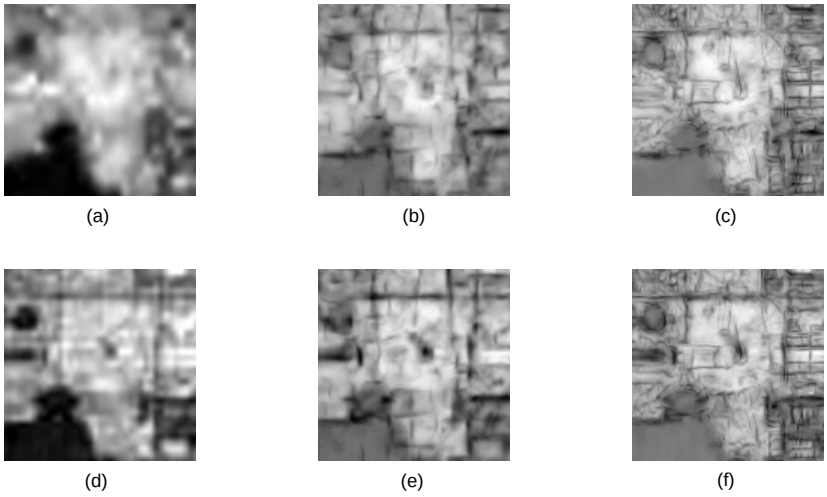

Figure 9: ROI images and fused phase maps: (a) Θ_1 ASTER, (b) ASTER plus $f(\mathbf{p}_1, \mathbf{p}_2)$, (c) ASTER plus $f(\bar{\mathbf{p}}_1, \bar{\mathbf{p}}_2, \bar{\mathbf{p}}_3)$. (d) Θ_2 Landsat, (e) Landsat plus $f(\mathbf{p}_1, \mathbf{p}_2)$, (f) Landsat plus $f(\bar{\mathbf{p}}_1, \bar{\mathbf{p}}_2, \bar{\mathbf{p}}_3)$.

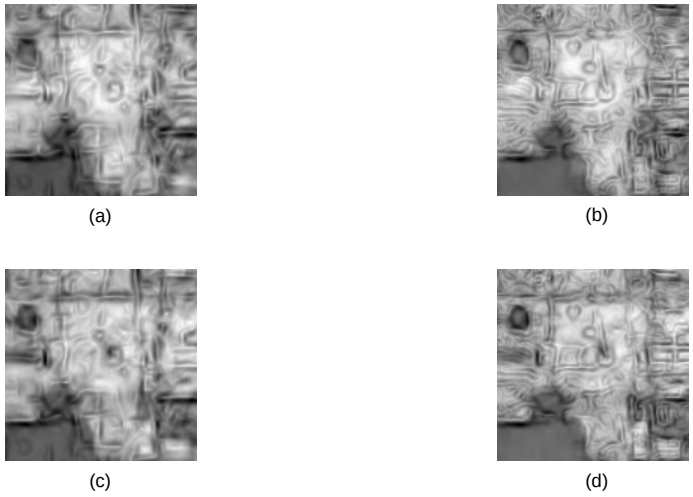

Figure 10: Gradients of Canny edge detection of fused phase maps: (a) ASTER plus gradient of $f(\mathbf{p}_1, \mathbf{p}_2)$, (b) ASTER plus gradient of $f(\bar{\mathbf{p}}_1, \bar{\mathbf{p}}_2, \bar{\mathbf{p}}_3)$. (c) Landsat plus gradient of $f(\mathbf{p}_1, \mathbf{p}_2)$, (d) Landsat plus gradient of $f(\bar{\mathbf{p}}_1, \bar{\mathbf{p}}_2, \bar{\mathbf{p}}_3)$.

4 Conclusions

In many digital imaging applications, multiple input images are acquired and some version of fusion is needed. An input mix of multimodal, multispectral, or multiresolution images is not uncommon. This paper describes a computational pipeline for image fusion in applications in which (1) input images are registered, sized, and scaled in pixel intensities suitably for mutual comparison, and (2) details about edges and lines are important information. When input images are packaged as a third-order tensor $\mathcal{A}$, HOSVD is a powerful decomposition tool. The basis images in the subtensor $\mathcal{B}$ found optimally by HOSVD are linear combinations of the inputs, orthogonal, and ordered by decreasing norm. Image phase analysis of these basis images is one way to extract details about edges and lines. Fusing the raw phase maps themselves by pixel-wise square root of the sum of the squares is consistent with the role of local energy in phase analysis. The fused maps can be added to inputs (or other images) for visualization or used for further image-related processing. (Further application-dependent processing is not a topic covered here. A particular application might mandate additional processing of images or phase maps or, at a more fundamental level, could call for a method other than phase analysis of the images in $\mathcal{B}$ in the first place.) If HOSVD has been computed for an initial set of images and additional images are acquired, incremental HOSVD is an effective way to update the decomposition, including the basis images. Reduced dimension HOSVD computed by HOOI results in smaller storage requirements and introduces an error that must be acceptable in an application; however, empirical results show that substantial reductions cause little degradation in visual quality in some cases.

Applications under development include multimodal tomography and multi-lens imaging with an emphasis on medical applications.

Acknowledgement
This work was partially supported by PERIODIC Workshops sponsored by DTO.

Appendix: Tensors and Higher-Order SVD

A.1. Summary of Notation and Basic Results

Refer to [1, 7, 8] for mathematical details of higher-order tensors, computations such as tensor-times-tensor product, and higher-order singular value decomposition (HOSVD). Let $\mathcal{A}$ denote an Nth-order tensor with dimensions $I_1, I_2, \ldots, I_N$. The *n-mode product* of $\mathcal{A}$ times an ordinary $(J_n \times I_n)$-matrix $\mathbf{U}$ is denoted by $\mathcal{A} \times_n \mathbf{U}$. This tensor-times-matrix product creates an Nth-order tensor with nth dimension equal to J_n and other dimensions the same as $\mathcal{A}$. If $J_n = I_n$, then $\mathcal{A} \times_n \mathbf{U}$ is the same size as $\mathcal{A}$ but in general does not have the same elements as $\mathcal{A}$ (the product $\mathcal{A} \times_n \mathbf{I}$ where $\mathbf{I}$ is the $I_n \times I_n$ identity matrix does equal $\mathcal{A}$). The *n-mode matrix unfolding* of $\mathcal{A}$, denoted by $\mathbf{A}_{(n)}$, is a conventional matrix with I_n rows, number of columns equal to the product $I_1 I_2 \cdots I_{n-1} I_{n+1} \cdots I_N$ of the non-n dimensions, and elements copied from $\mathcal{A}$ by cycling through the non-n indices in a fixed order (*backward cyclic* [7] or *forward cyclic* [15]). If Nth-order tensor $\mathcal{A}$ and Mth-order tensor $\mathcal{B}$ have the same n-mode dimension I_n, then the *n-mode tensor product* $\mathcal{A} \times_n \mathcal{B}$ creates a tensor of order $(N-1)+(M-1)$. If tensors $\mathcal{A}$ and $\mathcal{B}$ have identical dimensions, their tensor-times-tensor product over all N modes yields a tensor of order $2N - 2N = 0$. This zeroth-order tensor, which is a single real number, is the *scalar product* of $\mathcal{A}$ and $\mathcal{B}$ denoted $\langle \mathcal{A}, \mathcal{B} \rangle$. Two tensors for which $\langle \mathcal{A}, \mathcal{B} \rangle = 0$ are *orthogonal*. The *Frobenius norm* of a tensor $\mathcal{A}$ is

$$||\mathcal{A}|| = \sqrt{\langle \mathcal{A}, \mathcal{A} \rangle}$$

and its square $||\mathcal{A}||^2$ is the *energy in* $\mathcal{A}$. The squared norm $||\mathcal{A} - \mathcal{B}||^2$ for two same-sized tensors is the mean squared error (MSE). The Euclidean norm for matrix $\mathbf{A}$ is also denoted $||\mathbf{A}||$.

HOSVD is a generalization of conventional SVD [14] to higher orders. Theorem 2 in [7] is a characterization of tensor HOSVD summarized for real-valued tensors as follows:

Theorem. *Every* $(I_1 \times I_2 \times \cdots \times I_N)$*-tensor* $\mathcal{A}$ *can be written as the tensor-times-matrix product*

$$\mathcal{A} = \mathcal{S} \times_1 \mathbf{U}^{(1)} \times_2 \mathbf{U}^{(2)} \cdots \times_N \mathbf{U}^{(N)}$$

with the following characteristics:

1. *n-mode matrix* $\mathbf{U}^{(n)} = \left[U_1^{(n)}\ U_2^{(n)} \cdots\ U_{I_n}^{(n)}\right]$ *with column vectors* $U_i^{(n)}$ *is an orthogonal* $(I_n \times I_n)$*-matrix.*
2. *Core tensor* $\mathcal{S}$ *is an* $(I_1 \times I_2 \times \cdots \times I_N)$*-tensor of which the subtensors* $\mathcal{S}_{i_n=j}$*, obtained by fixing the nth index to* j*, have the properties of*

   (i) *all-orthogonality: two subtensors* $\mathcal{S}_{i_n=j}$ *and* $\mathcal{S}_{i_n=k}$ *are orthogonal if for all n, j, and k*

   $$\langle \mathcal{S}_{i_n=j}, \mathcal{S}_{i_n=k} \rangle = 0 \quad when \quad j \neq k,$$

   (ii) *ordering by decreasing norm:*

   $$||\mathcal{S}_{i_n=1}|| \geq ||\mathcal{S}_{i_n=2}|| \geq \cdots \geq ||\mathcal{S}_{i_n=I_n}|| \geq 0$$

   for all possible values of n.

The Frobenius norms $||\mathcal{S}_{i_n=j}||$*, symbolized by* $\sigma_j^{(n)}$*, are the n-mode singular values of* $\mathcal{A}$ *and the vector* $U_j^{(n)}$ *is a jth n-mode singular vector.*

See [7] for a proof of the theorem and an enumeration of several properties including the following.

Let the HOSVD of Nth order tensor $\mathcal{A}$ *be given as in the Theorem.*

• **Norm Property:** The *energy in* $\mathcal{A}$ *is related to the squared n-mode Frobenius norms as follows*:

$$\begin{aligned} ||\mathcal{A}||^2 &= \sum_{i=1}^{R_1} \sigma_i^{(1)^2} = \cdots = \sum_{i=1}^{R_N} \sigma_i^{(N)^2} \\ &= ||\mathcal{S}||^2. \end{aligned}$$

• **Oriented Energy Property:** The *n-mode oriented energy of* $\mathcal{A}$ in the direction of a unit-norm column vector X is the oriented energy of the complete set of n-mode vectors, i.e., is equal to the squared Euclidean norm

$$||X^T \mathbf{A}_{(n)}||^2.$$

The n-mode singular vectors $U_1^{(n)}, U_2^{(n)}, \ldots, U_{I_n}^{(n)}$ are the directions of the extremes of n-mode oriented energy and the corresponding extremal energy values are the squared n-mode singular values $\sigma_1^{(n)^2}, \sigma_2^{(n)^2}, \ldots, \sigma_{I_n}^{(n)^2}$.

A.2. Computation of HOSVD and Reduced Dimension HOSVD

Let $\mathcal{A}$ be an $(I_1 \times \ldots \times I_N)$-tensor and let its HOSVD be defined as in the Theorem. Each n-mode matrix $\mathbf{U}^{(n)}$ has orthonormal rows and orthonormal columns and its inverse is its transpose:

$$\mathbf{U}^{(n)^T} \mathbf{U}^{(n)} = \mathbf{U}^{(n)} \mathbf{U}^{(n)^T} = \mathbf{I}$$

where $\mathbf{I}$ is the identity matrix. The HOSVD of an Nth order tensor $\mathcal{A}$ can be computed [7, 8] by finding each matrix $\mathbf{U}^{(n)}$ of left singular vectors by standard SVD of the unfolded matrix $\mathcal{A}_{(n)}$, then using the matrix transposes $\mathbf{U}^{(n)^T}$ and tensor $\mathcal{A}$ to solve for the core tensor $\mathcal{S}$ as

$$\mathcal{S} = \mathcal{A} \times_1 \mathbf{U}^{(1)^T} \times_2 \mathbf{U}^{(2)^T} \times_3 \cdots \times_N \mathbf{U}^{(N)^T}.$$

The span of the left singular vectors $\mathbf{U}^{(n)}$ is the column space of the unfolded matrix $\mathbf{A}_{(n)}$ and the singular values $\sigma_i^{(n)}$ are the corresponding norms $||\mathcal{S}_{i_n=i}||$, $1 \leq i \leq I_n$.

A straightforward way to create a reduced dimension approximation $\hat{\mathcal{A}}$ of $(I_1 \times I_2 \times \cdots \times I_N)$-tensor $\mathcal{A}$ is by truncating or discarding parts of a full-dimensioned HOSVD, i.e., by computing the HOSVD for $\mathcal{A}$, then given the target dimensions $\kappa_n \leq I_n$, $1 \leq n \leq N$, reducing the size along each mode n by discarding the smallest n-mode singular values $\sigma_{\kappa_n+1}^{(n)}, \ldots, \sigma_{I_n}^{(n)}$ and deleting the corresponding parts of $\mathcal{S}$ and $\mathbf{U}^{(n)}$. This method is not guaranteed to minimize the MSE $||\mathcal{A}-\hat{\mathcal{A}}||^2$. By contrast, *higher-order orthogonal iteration* (HOOI) [8] searches for an approximation $\hat{\mathcal{A}}$ to minimize the MSE. HOOI is an alternating least squares method. It makes repeated passes through the reduced-size n-mode matrices $\mathbf{U}^{(1)}, \ldots, \mathbf{U}^{(N)}$, optimizing each matrix in turn within each pass while the other matrices are held constant, and recomputing the core tensor at the end of a pass.

HOOI can be used for tensors of any order. An iterative optimization specialized to rank-$(\kappa_1, \kappa_2, \kappa_3)$ approximation of a third-order tensor is given in [33] and applied to image analysis problems. The standard termination criteria for these iterative algorithms are that a maximum-iteration count is reached or an error measure falls below a threshold or stabilizes with no sign of further decrease.

References

[1] B. W. Bader and T. G. Kolda, "MATLAB Tensor Classes for Fast Algorithm Prototyping," *ACM Trans. Math. Software*, vol. 32, pp. 635-653, 2006.

[2] G. Bebis, A. Gyaourova, S. Singh, and I. Pavlidis, "Face Recognition by Fusing Thermal and Visible Imagery," *Image and Vis. Comp.*, vol. 24, pp. 727-742, 2006.

[3] R.S. Blum, "On Multisensor Image Fusion Performance Limits from an Estimation Theory Perspective," *Info. Fusion*, vol. 7, pp. 250-262, 2006.

[4] R.S. Blum, "Robust Image Fusion Using a Statistical Signal Processing Approach," *Info. Fusion*, vol. 6, pp. 119-128, 2005.

[5] M. Brand, "Incremental Singular Value Decomposition of Uncertain Data with Missing Values," *Proc. Eur. Conf. on Comp. Vis.*, Lecture Notes on CS, pp. 707-720, Springer-Verlag, 2002.

[6] J. Canny, "A Computational Approach to Edge Detection," *IEEE Trans. Pat. Anal. Mach. Intell.*, vol. 8, pp. 679-714, 1986.

[7] L. De Lathauwer, B. De Moor, and J. Vandewalle, "A Multilinear Singular Value Decomposition," *SIAM J. Matrix Anal. Appl.*, vol. 21, pp. 1253-1278, 2000.

[8] L. De Lathauwer, B. De Moor, and J. Vandewalle, "On the Best Rank-1 and Rank-$(R_1, R_2, \ldots, R_N)$ Approximation of Higher-Order Tensors," *SIAM J. Matrix Anal. Appl.*, vol. 21, pp. 1324-1342, 2000.

[9] S. Gabarda and G. Cristobal, "Cloud Covering Denoising through Image Fusion," *Image and Vis. Comp.*, vol. 25, pp. 523-530, 2007.

[10] B. Girod, "What's Wrong with Mean-Squared Error?," pp. 207-220 in *Digital Images and Human Vision*, MIT Press, Cambridge, MA, 1993.

[11] M. Gonzalez-Audicana, J.L. Saleta, R.G. Catalan, and R. Garcia, "Fusion of Multispectral and Panchromatic Images Using Improved IHS and PCA Mergers Based on Wavelet Decomposition," *IEEE Trans. Geoscience and Rem. Sen.*, vol. 42, pp. 1291-1299, 2004.

[12] A. A. Goshtasby, "Fusion of Multi-Exposure Images," *Image and Vis. Comp.*, vol. 23, pp. 611-618, 2005.

[13] A. A. Goshtasby and S. Nikolov, "Image Fusion: Advances in the State of the Art," *Info. Fusion*, vol. 8, pp. 114-118, 2007.

[14] M.T. Heath, *Scientific Computing: An Introductory Survey*, Second Ed., McGraw-Hill, NY, 2002.

[15] H. A. L. Kiers, "Towards a Standardized Notation and Terminology in Multiway Analysis," *J. Chemometrics*, vol. 14, pp. 105-122, 2000.

[16] S.G. Kong, J. Heo, F. Boughorbel, Y. Zheng, B.R. Abidi, A. Koschan, M. Yi, and M.A. Abidi, "Multiscale Fusion of Visible and Thermal IR Images for Illumination-Invariant Face Recognition," *Int'l. J. Comp. Vis.*, vol. 71, pp. 215-233, 2007.

[17] D. L. Kreider, R.G. Kuller, D.R Ostberg, and F.W. Perkins, *An Introduction to Linear Analysis*, Addison-Wesley, Reading, MA, 1966.

[18] P. Kovesi, "Image Features from Phase Congruency," *Videre: J. of Comp. Vis. Res.*, vol. 1, pp. 1-26, 1999.

[19] P. Kovesi, "Symmetry and Asymmetry from Local Phase," *Proc. 10th Australian Joint Conf. on AI (AI'97)*, Perth, December 2-4, 1997.

[20] S. Li, J.T. Kwok, and Y. Wang, "Combination of Images with Diverse Focuses Using the Spatial Frequency," *Info. Fusion*, vol. 2, pp. 169-176, 2001.

[21] S. Li, J.T. Kwok, and Y. Wang, "Using the Discrete Wavelet Frame Transform to Merge Landsat TM and SPOT Panchromatic Images," *Info. Fusion*, vol. 3, pp. 17-23, 2002.

[22] H. Li, B.S. Manjunath, and S.K. Mitra, "Multisensor Image Fusion Using the Wavelet Transform," *Graph. Models and Image Proc.*, vol. 57, pp. 235-245, 1995.

[23] B.J. Matuszewski, L-K Shark, M.R. Varley, and J.P. Smith, "Region-Based Fusion of Ultrasound, Radiographic, and Shearographic Non-Destructive Testing Images," *Proc. 15th WCNDT*, Rome, October 15-21, 2000.

[24] M. Muller, W. Kruger, and G. Saur, "Robust Image Registration for Fusion," *Info. Fusion*, vol. 8, pp. 347-353, 2007.

[25] G. Pajares and J. M. de la Cruz, "A Wavelet-Based Image Fusion Tutorial," *Pat. Recog.*, vol. 37, pp. 1855-1872, 2004.

[26] R. Plemmons, S. Prasad, S. Mathews, M. Mirotznik, R. Barnard, B. Gray, P. Pauca, T. Torgersen, J. van der Gracht, and G. Behrmann, "PERIODIC: Integrated Computational Array Imaging Technology," *Proc. Conf. on Comput. Optical Sen. and Imaging (COSI)*, Vancouver, June 18-20, 2007.

[27] C. Pohl and J.L.Van Genderen, "Multisensor Image Fusion in Remote Sensing: Concepts, Methods, and Applications," *Int'l. J. Remote Sen.*, vol. 19, pp. 823-854, 1998.

[28] G.M. Rojas, U. Raff, J.C. Quintana, I. Hiete, and M. Hutchinson, "Image Fusion in Neuroradiology: Three Clinical Examples Including MRI of Parkinson Disease," *Comp. Med. Imaging and Graphics,* vol. 31, pp. 17-27, 2007.

[29] G. Simone, A. Farina, F.C. Morabito, S.B. Serpico, and L. Buzzone, "Image Fusion Techniques for Remote Sensing Applications," *Info. Fusion*, vol. 3, pp. 3-15, 2002.

[30] J. Tanida, T. Kumagai, K. Yamada, S. Miyatake, K. Ishida, T. Morimoto, N. Kondou, D. Miyazaki, and Y. Ichioka, "Thin Observation Module by Bound Optics (TOMBO): Concept and Experimental Verification," *Appl. Opt.*, vol. 40, pp. 1806-1813, 2001.

[31] M. A. O. Vasilescu, "Human Motion Signatures: Analysis, Synthesis, Recognition," *Proc. Int'l. Conf. Pat. Recog. (ICPR'02)*, vol. 3, Quebec City, August 11-15, 2002.

[32] M. A. O. Vasilescu and D. Terzopoulos, "Multilinear Analysis of Image Ensembles: TensoFaces," *Proc. Eur. Conf. on Comp. Vis. (ECCV'02)*, Copenhagen, May 27-June 2, 2002.

[33] H. Wang and N. Ahuja, "Rank-R Approximation of Tensors Using Image-as-Matrix Representation," *Proc. IEEE Conf. Comp. Vis. and Pat. Recog. (CVPR'05)*, vol. 2, San Diego, June 20-25, 2005.

[34] Z. Wang, A.C. Bovik, H.R. Sheikh, and E.P. Simoncelli, "Image Quality Assessment: From Error Visibility to Structural Similarity," *IEEE Trans. Image Proc.*, vol. 13, pp. 600-612, 2004.